

Structure of homogeneous nonhelical magnetohydrodynamic turbulence

R. S. Miller,^{a)} F. Mashayek, V. Adumitroaie, and P. Givi

Department of Mechanical and Aerospace Engineering, State University of New York at Buffalo, Buffalo, New York 14260-4400

(Received 10 July 1995; accepted 24 May 1996)

Results are presented for three-dimensional direct numerical simulations of nonhelical magnetohydrodynamic (MHD) turbulence for both stationary isotropic and homogeneous shear flow configurations with zero mean induction and unity magnetic Prandtl number. Small scale dynamo action is observed in both flows, and stationary values for the ratio of magnetic to kinetic energy are shown to scale nearly linearly with the Taylor microscale Reynolds numbers above a critical value of $Re_\lambda \approx 30$. The presence of the magnetic field has the effect of decreasing the kinetic energy of the flow, while simultaneously increasing the Taylor microscale Reynolds number due to enlargement of the hydrodynamic length scales. For shear flows, both the velocity and the magnetic fields become increasingly anisotropic with increasing initial magnetic field strength. The kinetic energy spectra show a relative increase in high wave-number energy in the presence of a magnetic field. The magnetic field is found to portray an intermittent behavior, with peak values of the flatness near the critical Reynolds number. The magnetic field of both flows is organized in the form of "flux tubes" and magnetic "sheets." These regions of large magnetic field strength show a small correlation with moderate vorticity regions, while the electric current structures are correlated with large amplitude strain regions of the turbulence. Some of the characteristics of small scale MHD turbulence are explained via the "structural" description of turbulence. © 1996 American Institute of Physics. [S1070-664X(96)01009-9]

I. INTRODUCTION

Fifty years of widespread scientific investigation have passed since Kolmogorov's original theory of incompressible hydrodynamic (HD) turbulence.¹ Yet, due to its chaotic nature HD turbulence remains among the most complex unsolved problems in classical physics. Even more challenging is the problem of turbulence in electrically conducting fluids obeying the magnetohydrodynamic (MHD) equations.² Nonlinear coupling between the velocity and the magnetic induction fields produces many additional phenomena. In particular, production due to stretching and folding of field lines can lead to growth or sustainment of the magnetic field (the "MHD dynamo" effect^{3,4}). The production effect is a direct result of Maxwell's equations, i.e., an electromotive force is produced through Ohm's law when a conductor moves across magnetic field lines. Unbounded magnetic growth is prevented by the action of the Lorentz force on the velocity field resulting in a so-called saturated field condition.

Some of the earliest theoretical considerations of the dynamo problem suggest that the magnetic Reynolds number is one of the primary parameters in determining the strength (or lack) of field amplification and sustainment.³ Analytic studies of this phenomenon are performed by modeling the nonlinear terms,^{5,6} and by multiple scale analyses.⁷⁻⁹ These studies emphasize the importance of the magnetic helicity in amplifying the dynamo phenomenon. Other early studies enlist second order closure techniques to quantify this effect, and find that a magnetic steady state is achieved above a critical magnetic Reynolds number of order 30.¹⁰ The dy-

namo effect is difficult to observe in the laboratory due to the small values of the magnetic Prandtl number of available conducting fluids; see, e.g., Roberts and Hensen.¹¹ However, direct numerical simulation (DNS) offers a viable alternative to conventional laboratory experiments. Although current supercomputer technology limits DNS to moderate values of flow parameters (e.g., the Reynolds number) many important features of turbulence may be captured by such simulations.^{12,13}

One of the first three-dimensional (3-D) DNS of MHD turbulence is conducted by Pouquet and Patterson.¹⁴ They propose that large scale kinetic energy is transferred to high wave numbers through the traditional cascade process, where it is distributed between the velocity and the magnetic fields by Alfvén waves. In the presence of magnetic helicity the energy then follows an inverse cascade process from the small scales of the magnetic field to the large scales. Due to the turbulence decay, no validation of field sustainment is given; however, rapid field growth during early times of the simulation is observed. One of the first genuine nonlinear simulated dynamo effects is a convection driven dynamo in a spherical shell.¹⁵ This configuration is chosen to study some issues of importance to the solar dynamo. Meneguzzi, Frisch, and Pouquet¹⁶ study stationary isotropic turbulence and observe a small scale dynamo effect in the absence of helicity above a critical magnetic Reynolds number (of order 40). Several numerical simulations of 3-D MHD turbulence confirm that the magnetic Reynolds number is the primary parameter influencing the dynamo effect.^{10,15-17}

The scope of research pertaining to turbulence modification, intermittency, and coherent structures in MHD turbulence is somewhat limited. Most previous numerical simulations are confined to two-dimensional (2-D) flows. Biskamp,

^{a)}Present address: Jet Propulsion Laboratory, California Institute of Technology, Pasadena, California 91109-8099.

Welter, and Walter¹⁸ employ high resolution simulations of 2-D isotropic turbulence to address issues related to intermittency. By adapting the β model¹⁹ they conclude that while second order correlation functions are relatively unaffected by intermittency, the corrections necessary for fourth- and higher-order coefficients become significant. In addition, they observe departures from lognormality for small values of the local energy dissipation, a result in agreement with HD studies (e.g., Miller²⁰). Pouquet, Sulem, and Meneguzzi,²¹ incorporating both 2-D and 3-D simulations, illustrate how the correlations between the velocity and the magnetic fields can damp the energy exchange and reduce the amplitude and the intermittency of the derivative fields. Orszag and Tang²² find that the magnetic field is more intermittent than the velocity field in 2-D MHD turbulence. This observation is verified in 3-D flows for the thermal convection problem,¹⁷ and also in isotropic turbulence.¹⁶ Intermittent magnetic field regions organize into magnetic “flux tube” structures similar to the vorticity tubes of hydrodynamic turbulence. These magnetic structures are observed in 3-D MHD simulations of isotropic turbulence,¹⁶ high symmetry turbulence employing hyperviscosity and hypermagnetic diffusivity,²³ and in compressible stratified convection above a stable overshoot layer.^{24,25}

Although a zero mean magnetic field can be sustained through dynamo action, most MHD flows in nature occur with a mean field. The mean field is typically “slowly” varying with respect to the dynamic fluctuations. Thus, in some cases, it is possible to consider the mean field to be locally steady and uniform. The most obvious effect of a mean magnetic field is to create an anisotropic turbulence state for both the velocity and the magnetic fields. The Lorentz force has zero component parallel to the induction field, and anisotropic states occur due to less restriction of fluid motions parallel to the mean. Shebalin, Matthaeus, and Montgomery²⁶ and Oughton, Priest, and Matthaeus²⁷ investigate the influence of a mean magnetic field in both 2-D and 3-D homogeneous flow simulations. Their results indicate that an externally applied dc field preferentially transfers energy to modes with wave vectors perpendicular to the mean field and also inhibits the development of turbulence. These observations indicate that traditional “return to isotropy” theories may not be applicable to the small scales of naturally occurring MHD turbulence, and that increased understanding of anisotropic MHD turbulence is warranted.

In this article, results are presented of DNS of 3-D homogeneous magnetohydrodynamic turbulence for both stationary isotropic and homogeneous shear flow configurations. For simplicity, only incompressible nonhelical velocity fields and zero mean magnetic fields with magnetic Prandtl number equal to unity are considered. However, many important features of MHD turbulence are captured, including small scale dynamo action, equipartition of energies in the small scales, and effects of the Lorentz force on the velocity field. All MHD simulations are repeated for the case of HD turbulence. The homogeneous shear flow is a relatively simple configuration, and is convenient for the study of anisotropic MHD turbulence in the absence of a mean magnetic field. The specific objectives of the study are to (1) assess

modifications to the turbulence due to the magnetic field, (2) quantify the dynamo effect in both isotropic and homogeneous shear flows, and (3) investigate some issues of importance in relation to coherency and intermittency in MHD turbulence.

II. FORMULATION AND PARAMETRIZATION

The incompressible form of the MHD equations are employed to describe the turbulent transport in both isotropic and homogeneous shear “box” flows. The nondimensional MHD equations for the fluctuation fields (zero mean) are considered in conservative form:

$$\frac{\partial u_j}{\partial x_j} = 0, \quad \frac{\partial b_j}{\partial x_j} = 0, \quad (1)$$

$$\frac{\partial u_i}{\partial t} + \frac{\partial}{\partial x_j} (u_i u_j) = - \frac{\partial p^t}{\partial x_i} + \frac{\partial}{\partial x_j} (b_i b_j) + \frac{1}{\text{Re}_0} \frac{\partial^2 u_i}{\partial x_j \partial x_j} + f_i, \quad (2)$$

$$\frac{\partial b_i}{\partial t} + \frac{\partial}{\partial x_j} (b_i u_j) = \frac{\partial}{\partial x_j} (u_i b_j) + \frac{1}{\text{Re}_{0m}} \frac{\partial^2 b_i}{\partial x_j \partial x_j}. \quad (3)$$

Here u_i ($i=1,2,3$) denotes the components of the velocity vector \mathbf{u} (boldface indicates a vector), b_i represents the components of the magnetic induction vector \mathbf{b} , and p^t denotes the total pressure. The transport variables are normalized with respect to the reference length (L_0), velocity (U_0), induction (B_0), and density (ρ_0) scales. The nondimensional diffusivity is the inverse of the “box Reynolds number,” $\text{Re}_0 = U_0 L_0 / \nu$, where ν is the kinematic viscosity. The box magnetic Reynolds number is defined as $\text{Re}_{0m} = U_0 L_0 / \nu_m = \text{Pr}_m \text{Re}_0$, where the ratio of kinetic to magnetic diffusivities is denoted by the magnetic Prandtl number, $\text{Pr}_m = \nu / \nu_m$. In Eq. (2), f_i is a forcing term to be discussed below.

Simulations are conducted of both stationary isotropic and homogeneous shear turbulence within the domain $0 \leq x_i \leq L = 2\pi$ ($x_1 \equiv x$, $x_2 \equiv y$, $x_3 \equiv z$). A Fourier pseudospectral method with triply periodic boundary conditions is employed for the spatial discretization of all transport variables. All calculations are performed in Fourier space with the exception of the nonlinear terms, and time advancement is performed using an explicit second order accurate Adams–Bashforth technique. The computational routine is capable of simulating both stationary or decaying isotropic, and homogeneous shear flows for either the HD ($\mathbf{b} \equiv \mathbf{0}$) or the MHD equations. The computational requirement for the solution of the Navier–Stokes equations (on a Cray-C90 supercomputer) is approximately 0.18, 0.60, 1.25, and 4.80 s per iteration for 32^3 , 48^3 , 64^3 , and 96^3 collocation points, respectively. For the full MHD equations, 0.40, 1.35, 3.2, and 10.8 s per iteration are required for the same respective resolution.

To emulate the stationary isotropic turbulence field, a low wave-number forcing scheme is imposed. This is implemented by adding energy to the large scales of the turbulence at a statistically constant rate, whereby an energy cascade is developed for sufficiently large Reynolds numbers. The energy is then dissipated at high wave numbers at the same rate and a statistically stationary state is achieved. Provided that

there is sufficient separation between the low and high wave numbers, the small scale turbulence is considered to be unaffected by the artificial forcing. The forcing algorithm employed is based on a scheme developed by Eswaran and Pope²⁸ and is described in detail by Miller.²⁰

In homogeneous shear turbulence simulation, a linear mean velocity profile is added to the fluctuating velocity. The primary effect of the mean shear is to provide a natural (albeit idealistic) homogeneous forcing. In contrast to the isotropic case, no stationary state is achieved and the Reynolds number grows until the turbulence structures outgrow the box size. The magnitude of the imposed shear is given with the amplitude of the mean gradient, in this case $Y = dU_1/dx_2 = \text{const}$ (where U_1 denotes the mean component of the velocity in the $i=1$ direction). In order to use the Fourier spectral method, the governing equations are solved for their fluctuating quantities on a grid which deforms with the mean flow. The transformation is an extension of the procedure employed by Rogallo²⁹ for HD turbulence and details of its implementation of MHD flows are provided by Miller.²⁰ The mean shear imposed by the grid transformations skews the grid in time. In order to allow the simulation to progress for a substantial time, it is necessary to remesh the grid at regular intervals. Aliasing errors introduced by the remesh process are removed via a truncation of the variables in Fourier space outside of the spherical wave-number shell of magnitude $\sqrt{2}N/3$, where N is the number of collocation points in any direction. This results in a slight loss of kinetic and magnetic energy; however, if the simulation is well resolved this truncation is considered to be negligible. The simulations are performed until the length scales of the turbulence become too large to be accurately resolved, at which time the simulation is terminated.

Both the velocity and magnetic fields are initialized as random Gaussian, isotropic, and solenoidal fields. Non-mirror-symmetric \mathbf{b} fields with arbitrary magnetic helicities are generated by the method described in Pouquet and Patterson.¹⁴ The relative magnitude of the helicity is specified through the correlation coefficient of the \mathbf{b} field and its vector potential \mathbf{a} ($\mathbf{b} = \nabla \times \mathbf{a}$): This coefficient is defined as $C(\mathbf{a}, \mathbf{b}) = \langle a_i b_i \rangle / \sqrt{\langle a_j a_j \rangle \langle b_k b_k \rangle}$, where the angular brackets ($\langle \rangle$) indicate an ensemble average over all grid points. The initial energy for the velocity is $E_v = \langle u_i u_i \rangle = 3$ in all cases. The forcing amplitude ($A_F = 1.25$), forcing radius ($K_F = 2\sqrt{2}$), and the magnitude of the mean velocity gradient ($Y = 2$) are kept fixed for the respective flows. In the isotropic simulations, an initial kinetic energy spectrum having $E'_v(k) \sim k^{-5/3}$ (the prime indicates the energy spectra as a function of the wave-number magnitude) is imposed. This choice is somewhat arbitrary since the asymptotic statistical state of the turbulence is independent of the initial conditions, and is primarily dependent on the forcing parameters and the box Reynolds number. For the shear (SHR) flow simulation cases, the velocity field and all of the magnetic fields are specified with a spectrum $\sim k^4 \exp[-2(k/k_s)^2]$, where the parameter k_s specifies the wave-number location for the maximum amplitude of the energy spectrum. The value $k_s = 7$ is chosen for the initial velocity spectrum in all shear simulations, whereas k_s is varied for the magnetic fields in

TABLE I. Conditions for the ISO simulations. All simulations are repeated with $E_m = 0$.

	Re_0	E_M/E_V	k_s	$C(\mathbf{a}, \mathbf{b})$	N	$\Delta t (\times 10^{-3})$	t_{final}	τ_e	ηk_{max}
IRun0	200	0.01	7	0	96	2.5	45	1.80	1.65
IRun1	150	0.01	7	0	64	3.75	56	1.51	1.28
IRun2	150	1.00	7	0	64	3.75	56	1.50	1.24
IRun3	150	0.01	2	0	64	3.75	56	1.51	1.29
IRun4	150	0.01	7	1	64	3.75	56	1.49	1.22
IRun5	110	0.01	7	0	64	3.75	70	1.41	1.48
IRun6	60	0.01	7	0	48	5.0	70	1.33	1.43
IRun7	40	0.01	7	0	48	5.0	120	1.47	1.84
IRun8	20	0.1	7	0	32	7.5	150	1.52	1.98
IRun9	10	0.1	7	0	32	7.5	150	2.07	3.33

order to study its influence. Detailed studies of the effects of both the initial conditions and the rate of shear have been conducted by Rogallo²⁹ for HD flows.

A listing of all the simulation parameters are provided in Table I for the isotropic (ISO) flow simulations and in Table II for the SHR flow simulations. The labels in the first column of each table are preceded by ‘I’ and ‘S’ for the ISO and the SHR flow simulations, respectively. The information listed for each simulation includes the box Reynolds number (Re_0), the ratio of initial magnetic and kinetic energies (E_m/E_v , where $E_m = \langle b_i b_i \rangle$), the wave number of maximal initial magnetic energy (k_s), the magnetic helicity, the grid resolution, the time step, the duration of simulation, the eddy turnover time (τ_e), and the resolution parameter (ηk_{max}). The eddy turnover time is defined as the ratio of the integral length scale to a characteristic velocity:

$$\tau_e = \frac{\Lambda}{u_{\text{rms}}}, \quad \Lambda = \frac{3\pi}{2E_v} \int_0^{k_{\text{max}}} \frac{E'_v(k)}{k} dk, \quad (4)$$

where the subscript rms denotes the root mean square (u_{rms} is calculated as the average of the rms of all three velocity components) and Λ is the integral length scale. The resolution parameter is the product of the Kolmogorov length scale [$\eta = (\nu^3/\langle \epsilon \rangle)^{1/4}$, $\epsilon = 2\nu s_{ij} s_{ij}$, where the symmetric rate of strain tensor is $s_{ij} = (u_{i,j} + u_{j,i})/2$ and the derivative notation is $u_{i,j} = \partial u_i / \partial x_j$] and the maximum resolved wave number (k_{max}). The box Reynolds number, the grid resolution, and the time step are held constant for the SHR flow simulations and take the values $Re_0 = 200$, $N = 96$, and $\Delta t = 2.5 \times 10^{-3}$. For all cases the magnetic Prandtl number is $Pr_m = 1$, in which case η represents the smallest length scale of both the turbulence and the magnetic field. The values given for both τ_e and ηk_{max} correspond to time averaged values for the

TABLE II. Conditions for the SHR simulations, $Re_0 = 200$, $N = 96$, $\Delta t = 2.5 \times 10^{-3}$.

	E_M/E_V	k_s	$C(\mathbf{a}, \mathbf{b})$	t_{final}	τ_e	ηk_{max}
SRun0	5	1.05	1.16
SRun1	0.01	7	0	6	1.18	1.26
SRun2	0.1	7	0	6	1.48	1.45
SRun3	1.00	7	0	6	2.06	1.74
SRun4	0.01	2	0	6	1.39	1.34
SRun5	0.01	7	1	6	1.17	1.25

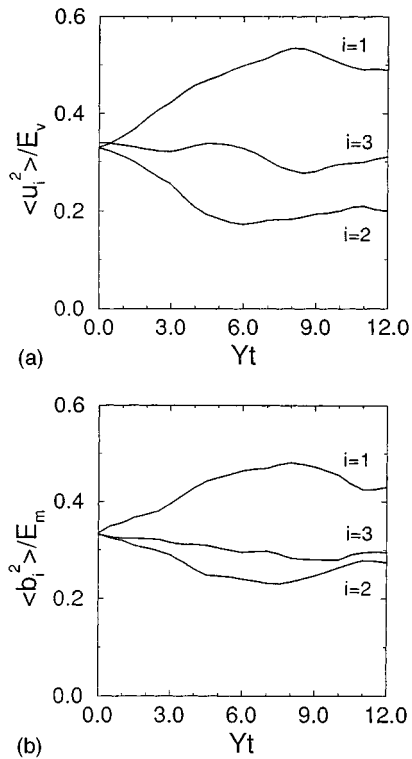


FIG. 1. Temporal evolution of the relative component energies for the homogeneous shear simulation SRUn1: (a) kinetic energy, (b) magnetic energy.

stationary ISO runs in the presence of the magnetic field. For the SHR simulations, these parameters are given at the time when the relative energy of the u_1 velocity component reaches its maximal value (discussed below). All of the ISO MHD cases corresponding to different Re_0 values are repeated with purely HD flow, and SRUn0 represents a purely HD case having the same parameters as cases SRUn1–SRUn5.

III. RESULTS

In each of the ISO simulations, the equations governing the hydrodynamics are first integrated forward in time for a minimum of five eddy turnover times to reach a stationary state. At this time, the magnetic field is added to begin the simulation or, in the HD cases, the integration is continued for more than 10 eddy turnover times to calculate time averaged statistics. The MHD simulations are conducted for a sufficient duration to determine the existence of stationary magnetic states. Those simulations which attain stationary states are continued for more than 10 additional eddy turnover times so that time averaging can be performed on the data. Time is normalized by the HD eddy turnover time (t/τ_e) for the ISO flow simulations.

For the SHR flow cases, the mean shear is directly applied to the initial isotropic fields. No stationary states exist in this flow; however, energy component ratios (relative energies) are known to attain approximate “asymptotic” values as indicated in previous HD simulations (e.g., Rogers and Moin³⁰). This is observed to be the case in the MHD flow also. Figure 1 portrays an example of this effect for case

SRUn1 (time is normalized via the mean shear magnitude for the SHR flow simulations). The relative energy of a vector component is defined as the ratio of the variance of that particular component relative to the total vector energy, i.e., $\langle u_i^2 \rangle / E_v$ and $\langle b_i^2 \rangle / E_m$. The time at which the ratio $\langle u_1^2 \rangle / E_u$ reaches a maximum value is denoted as the “peak time.” Note that the relative energies of all components of both the \mathbf{u} and \mathbf{b} fields are initially about $\frac{1}{3}$, due to the initial isotropic conditions.

Comprehensive resolution studies have been conducted to assess the effects of grid resolution on both the time averaged ISO simulation statistics and on the temporal evolution for the SHR flows. Two of the low Reynolds number cases, IRun6 and IRun8, were repeated with 16^3 , 24^3 , 32^3 , 48^3 , and 64^3 grid points and case IRun1 was repeated with 32^3 , 48^3 , and 96^3 grid points. In addition, the SHR flow resolution was investigated by repeating case SRUn1 with 48^3 , 64^3 , and 128^3 grid points. In all cases, the magnetic field moments are more sensitive to resolution than the equivalent statistics of either the velocity field or its gradients. An evaluation of statistical moments as large as fourth order reveals that the parameter ηk_{\max} is the primary parameter for the resolution consideration. Results from the larger Reynolds number ISO and SHR cases indicate that adequate resolution is obtained for $\eta k_{\max} \approx 1.2$ and larger. This is in agreement with previous findings in the case of HD stationary turbulence.²⁸ However, for smaller ISO grid sizes (IRun6 and IRun8) a larger resolution is necessary to yield accurate statistics for the magnetic field; $\eta k_{\max} \approx 1.4$ and larger. This is a result of the relatively small separation between the smallest scales of the turbulence and the forcing scales. All of the results indicate that the simulations listed in the tables are sufficiently resolved, and the results presented hereinafter are independent of the grid size.

A. Effects of initial conditions

For both the ISO and SHR simulations, a variety of initial conditions are considered to study the effects of the initial ratio of the magnetic and hydrodynamic energies, the initial length scale of the magnetic field, and the initial magnetic helicity on flow evolutions. This is particularly important in the ISO simulations, as it is important to establish that stationary states are independent of initial conditions before making quantitative comparisons. The SHR flow does not relax to a steady state condition; therefore, it is expected that the effects of initial conditions will prevail throughout the simulated times considered here.

Simulations IRun1 through IRun4 are considered to establish the independence of ISO steady state results to initial conditions. Figure 2 presents the time evolution of both the energy ratio (E_m/E_v) and the magnetic enstrophy ($H_m = \langle j_i j_i \rangle$, where $\mathbf{j} = \nabla \times \mathbf{b}$ is the electric current density) for a duration of approximately 37 eddy turnover times. It appears that both quantities asymptotically approach the steady state condition. Analysis of other quantities (not shown here) confirms that this is the case. However, the early temporal evolutions are highly dependent on the initial \mathbf{b} fields. Figure 2 is also useful in assessing the effects of the initial conditions at early times. Simulations IRun1 and

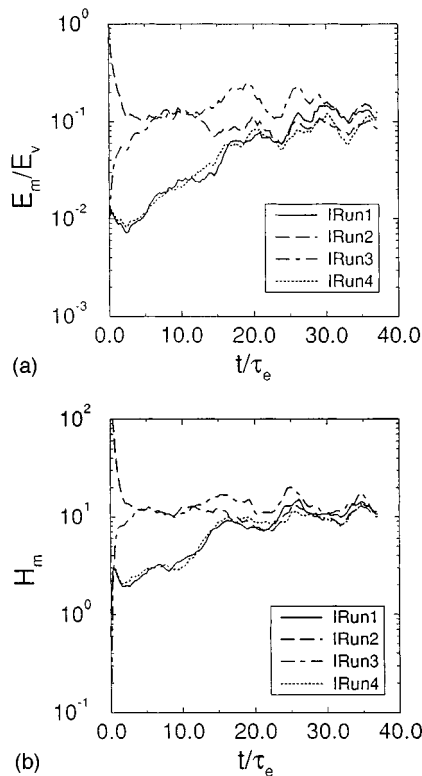


FIG. 2. Effect of initial conditions on the stationary isotropic simulations as shown by the temporal evolutions of (a) the energy ratio and (b) the magnetic enstrophy.

IRun3 contain initially relatively small scale ($k_s=7$) and large scale ($k_s=2$) magnetic fields, respectively, and otherwise have identical parameters [$E_m/E_v=0.01$ and $C(\mathbf{a},\mathbf{b})=0$]. The early time behavior of both the energy ratio and the magnetic enstrophy exhibits substantially larger initial growth rates for the large scale \mathbf{b} field (IRun3). The expected value of the magnetic dissipation is the primary parameter affecting the early time evolutions of these fields. The relatively large energy at high wave numbers in simulation IRun1 results in a mean dissipation which is more than an order of magnitude larger than that of IRun3 with an initially large scale field (the respective values are $\langle \epsilon_m \rangle = \nu_m \langle b_{i,j} b_{i,j} \rangle = 6.81 \times 10^{-3}$ and 6.38×10^{-4}).

The early time effects of initial magnetic helicity are also illustrated in Fig. 2 by the data of simulations IRun1 and IRun4. The temporal evolutions of both the energy ratio and the magnetic helicity are nearly independent of the initial magnetic helicity. This is due to the absence of any mechanism by which the magnetic helicity can be supported. The correlation between the \mathbf{b} field and its potential in simulation IRun4 decreases to less than 10% of its initial value in less than two eddy turnover times. Note that case IRun2 with an initial unity energy ratio is observed to decay rapidly towards the same approximate stationary state as cases IRun1, IRun3, and IRun4. The long time fields are thus considered to be independent of initial conditions and, of these runs, only the time averaged data of simulation IRun1 are considered in the remainder of the article.

The above discussion of the early time effects of the

magnetic field initial conditions is also applicable to the SHR configuration. However, in these flows the hydrodynamic field also experiences rapid modifications at early times due to the action of the applied mean velocity gradient, and no stationary state exists. Due to the action of the Lorentz force, additional initial condition effects with regard to turbulence modification are expected. As such, the effects of initial conditions are felt throughout the simulations.

B. Integral flow statistics

For the ISO cases, the statistical analyses of the data are most often conducted in terms of both spatial and temporal averaging (when stationary states exist). Statistics gathered from several simulations can be used to study the effects of the flow parameters. There are a number of choices by which to parametrize the problem, including the box size, the integral length scale, and the Taylor microscale Reynolds numbers (Re_λ), etc. Analysis of the data indicates that Re_λ yields the most insight into the problem. For SHR flows Re_λ is based on the Taylor microscale (λ_1) in the x_1 direction ($\lambda_\alpha^2 = \langle u_\alpha^2 \rangle / \langle (\partial u_\alpha / \partial x_\alpha)^2 \rangle$) (no summation over repeated Greek indices hereinafter) and the turbulent velocity scale ($\sqrt{E_v}$). For ISO flows the Reynolds number is defined as the average over all three directions x_ξ with corresponding length and velocity scales λ_ξ and $\sqrt{\langle u_\xi^2 \rangle}$, respectively. Results for the SHR runs are presented as both temporal evolutions and occasionally in the form of tabular data at the peak times of the simulations.

Leorat, Pouquet, and Frisch¹⁰ find a bifurcation to a magnetic state in their eddy damped quasinormal Markovian (EDQNM) approximation study of nonhelical MHD turbulence above a critical magnetic Reynolds number of a few tens. Figure 3 presents both the Reynolds number (in ISO) and temporal (in SHR) dependence of the kinetic, the magnetic and the total ($E_t = E_v + E_m$) energies. The data in both figures are normalized by the kinetic energy of the purely HD flow (SRun0 for the SHR flow). The ISO results are in good qualitative agreement with the EDQNM predictions¹⁰ and show a transition to ‘‘magnetic states’’ occurring at a critical Reynolds number of $Re_{\lambda,c} \approx 30$. Above this critical value, sustained \mathbf{b} fields are observed, and both the kinetic and total energies decrease with the Reynolds number. The transition is more gradual in the present results than that predicted by the EDQNM approximation. The SHR data correspond to case SRun4 having a large scale initial \mathbf{b} field with 1% energy ratio. In this simulation, the initial seed magnetic field is rapidly amplified in the early stages of development and then gradually decreases. Note that no conclusions can be made from this figure in regard to a sustained dynamo effect for the SHR simulation. This is because the energies are normalized by the kinetic energy of the HD simulation. However, these results do illustrate several effects of the \mathbf{b} field. In both the ISO and the SHR cases the presence of the magnetic field acts to damp the turbulence energy (also observed in all the other SHR simulations). In addition, the normalized kinetic energy for the SHR simulation reaches a nearly constant value after $Yt \approx 2$.

Time averaged values of the steady state ISO energy

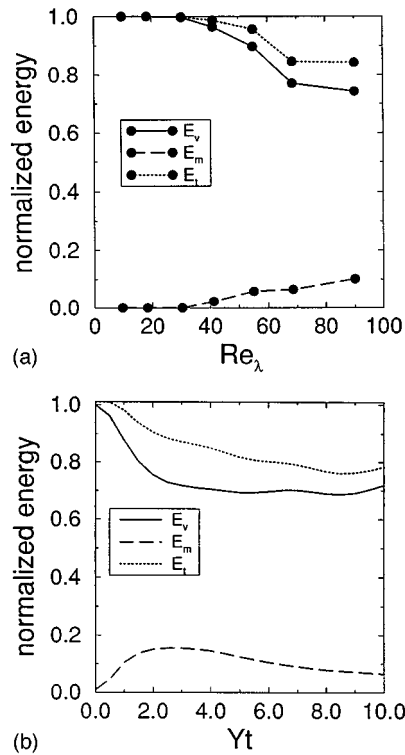


FIG. 3. Development of the kinetic, magnetic, and total energies as normalized by the purely hydrodynamic kinetic energy E_v (HD), (a) ISO simulation time averaged results as a function of the Reynolds number for cases IRun0, 1, 5, 6, 7, 8, and 9 (right to left) and (b) temporal evolution of SHR simulation, case SRun4.

ratios in MHD turbulence are listed in Table III as a function of various Reynolds numbers (the normalization is with the MHD E_v). The ratios for the higher Reynolds number cases ($E_m/E_v \sim 0.1$ for $Re_\lambda \approx 100$) are in accord with the results of Meneguzzi, Frisch, and Pouquet.¹⁶ When presented graphically (not shown), the energy ratios portray a nearly linear dependence on the Taylor microscale Reynolds number for the range of parameters considered. A very weak magnetic field is sustained for case IRun7 with $Re_\lambda = 30.3$ (for more than 100 HD eddy turnover times), while the two simulations with lower Reynolds numbers do not support a magnetic field. The magnetic energy in simulation IRun8 was allowed to decay to a value of $E_m/E_v \sim 10^{-25}$ and no evidence of a magnetic steady state was observed. Based on these observations, the critical value of the Reynolds number for small scale dynamo action is concluded to be $Re_{\lambda,c} \approx 30$ (or $Re_{\Lambda,c} \approx 55$).

TABLE III. Time averaged values for the ratio of magnetic to kinetic energy for the ISO flow simulations.

	Re_0	Re_λ	Re_Λ	E_m/E_v
IRun9	10	9.66	13.8	...
IRun8	20	18.4	31.2	...
IRun7	40	30.3	55.6	2.0×10^{-4}
IRun6	60	41.2	79.9	2.3×10^{-2}
IRun5	110	55.0	118	6.5×10^{-2}
IRun1	150	68.5	150	1.2×10^{-1}
IRun0	200	90.0	205	1.6×10^{-1}

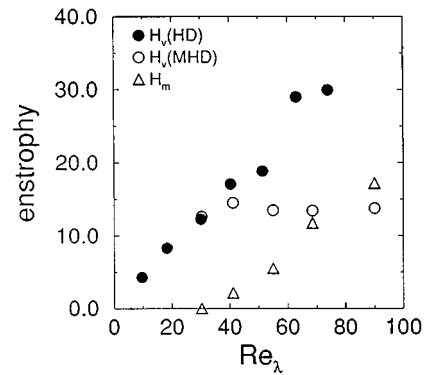


FIG. 4. Reynolds number dependence of the kinetic and the magnetic enstrophy for the ISO simulations IRun0, 1, 5, 6, 7, 8, and 9 (right to left).

The transition to magnetic states is characterized by several changes in both the hydrodynamic and the electromagnetic structure of the flow field. In particular, the kinetic and magnetic enstrophies provide a measure of the respective rotational and electric current density energies of the velocity and the magnetic fields (the kinetic enstrophy is defined as $H_v = \langle \omega_i \omega_i \rangle$, ω is the vorticity vector). Figure 4 depicts these quantities as a function of Re_λ for the steady state values of the ISO simulations. This figure indicates a significant drop in H_v in the presence of a sustained dynamo effect. The HD data show a near linear rise in H_v over the range of Reynolds numbers simulated. However, the MHD flow shows an apparent plateau value of the kinetic enstrophy for Reynolds numbers above the critical value. As the ratio of the magnetic to kinetic energy grows, the Lorentz force becomes increasingly significant to small scale flow dynamics. As will be shown later, this force tends to align perpendicular to the vorticity vector and acts to disperse high vorticity regions of the turbulence, hence decreasing the kinetic enstrophy. Figure 4 also shows that the magnetic enstrophy increases steadily for $Re_\lambda > Re_{\lambda,c}$ and eventually becomes larger than H_v . This trend is observed in spite of the fact that the largest energy ratio observed in the ISO simulations is “only” about 15% (see Table III). The larger magnetic enstrophy in comparison to the kinetic enstrophy is due to a more intermittent behavior of the magnetic field in comparison to the velocity field.

Significant insight into MHD small scale dynamics and intermittency is gained by the examination of the higher order statistics of the field variables and their derivatives. These statistics are important in characterizing the transition to magnetic states. The skewness and flatness of a zero mean random variable v_ξ are defined as $\mu_3(v_\xi) = \langle v_\xi^3 \rangle / \langle v_\xi^2 \rangle^{3/2}$ and $\mu_4(v_\xi) = \langle v_\xi^4 \rangle / \langle v_\xi^2 \rangle^2$, respectively. In agreement with previous HD and MHD studies,^{31,32} the velocity field is found to be nearly Gaussian for all flow fields considered, while the statistics of both the velocity and magnetic fields and their longitudinal derivatives are observed to be symmetrically distributed about the mean (i.e., zero skewness). The time averaged flatness values of the magnetic field are presented in Fig. 5 for the ISO simulations (presented as the average of the three coordinate components). Below the critical Reynolds number ($Re_{\lambda,c} \approx 30$) the dynamo effect is not present,

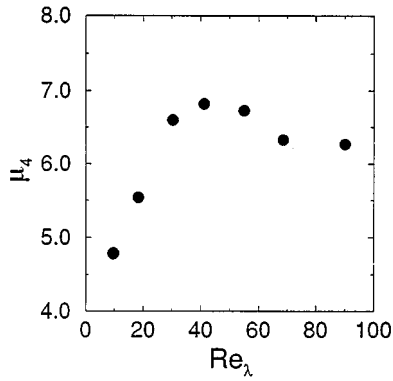


FIG. 5. Reynolds number dependence of the flatness factor for the magnetic field for the ISO simulations IRun0, 1, 5, 6, 7, 8, and 9 (right to left).

but the magnetic field maintains an approximate “self-similar” decay and time averaged flatness values are calculated. In these low Reynolds number cases, the flatness factors for the \mathbf{b} field are observed to be considerably larger than that of Gaussian. The flatness for the \mathbf{b} field exhibits a maximum value at $Re_\lambda \approx 40$ and then decreases. It is suggested that this can be explained in terms of the energy ratio. In the next section it is shown that the crossing point (equipartition) of the kinetic and the magnetic energy spectra moves towards lower wave numbers as the Reynolds number and the energy ratios are increased. The magnetic stretching term in the transport equation for the \mathbf{b} field is the inner product of a large scale field (\mathbf{b}) with a hydrodynamic dissipation scale gradient term. Therefore, as the relative strength of the \mathbf{b} field is increased and the corresponding equipartition wave number migrates away from the dissipation scales, the magnetic field stretching term in Eq. (3) appears more “space filling” (less intermittent). For Reynolds numbers below the critical value, the primary scales for interactions between the magnetic field and the velocity field are the dissipation scales. In this case, the magnetic field intermittency therefore increases with the magnetic field strength. Additional larger Reynolds number simulations are needed to investigate the fate of the magnetic flatness at large Reynolds numbers.

Some insight into the existence of a dynamo effect for SHR simulations is gained by examining the evolutions of the energy ratio and the magnetic energy (normalized by its initial value), as shown in Fig. 6. All \mathbf{b} fields except the unity energy ratio case (SRun3) experience an initial rise in energy due to the abrupt application of the mean velocity gradient at time $Yt=0$. This causes strong stretching and bending effects on the initial random magnetic fields, and hence amplification of the magnetic energy. Simulation SRun3 has a sufficiently large energy to resist these effects and actually damps the \mathbf{u} field to a large enough extent to display no initial magnetic energy growth [Fig. 6(b)]. The sharpest relative increase in magnetic energy occurs for the large scale initial field of SRun4 with nearly an order of magnitude increase within the first large scale turnover time. The positive growth rates of the magnetic energies observed in the latest stages of the simulations (except SRun3) in Fig. 6(b) suggest the presence of a dynamo effect. The rates of growth of the magnetic

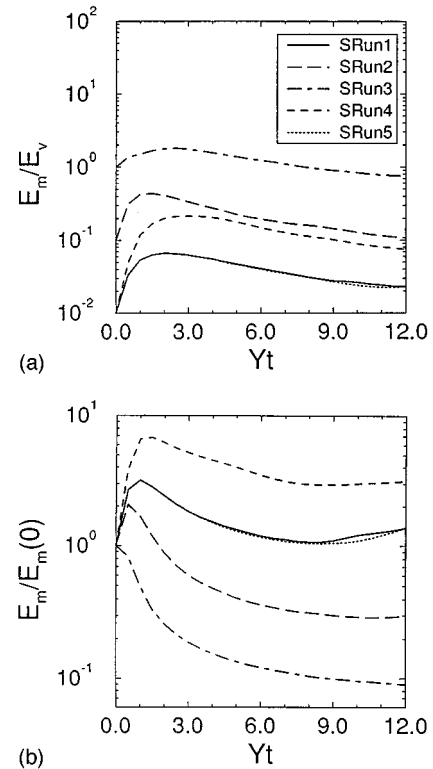


FIG. 6. Temporal development of the energies for the SHR simulations: (a) the energy ratio, and (b) the magnetic energy normalized by the initial value. The legends are the same for both figures.

fields are slower than those of the velocity field, as evidenced by the monotonically decreasing energy ratios at later times in Fig. 6(a).

Some results portraying the anisotropy of the SHR flow are presented in Table IV. This table lists various statistics of both the HD and MHD flows. Previous DNS data of Rogers and Moin³⁰ (RM) are also included for comparison. The correlation coefficient in the table is defined as $C(v_\alpha, v_\beta) = \langle v_\alpha v_\beta \rangle / \sqrt{\langle v_\alpha^2 \rangle \langle v_\beta^2 \rangle}$ for the vector \mathbf{v} . The addition of a magnetic field delays the turbulence development and results in the increased peak times used for comparisons. The table suggests that an important parameter influencing the anisotropy and the Reynolds stress development is the instantaneous energy ratio at the peak times. Notwithstanding SRun4, as the instantaneous energy ratio is increased, the primary effects on the turbulence are to increase the anisotropy of both the velocity and the magnetic fields and also to decrease the magnitude of the Reynolds number. The case SRun4 is initialized with a relatively large scale (“force-free”) magnetic field and is able to develop the largest value of the Reynolds number despite having a moderate energy ratio. The reason for the increase in anisotropy with the energy ratio is that the Lorentz force exhibits preferred orientations in the x_2 - x_3 plane. Therefore, this force causes the relatively largest resistance to fluid motions in directions perpendicular to the streamwise direction, thus increasing the fluid anisotropy. This preferential orientation of the Lorentz force is discussed in Sec. III D. Table IV also illustrates that the correlation $C(u_1, u_2)$ decreases as the energy ratio is

TABLE IV. Comparisons of instantaneous parameters for the SHR simulations at the peak times.

	RM	SRun0	SRun1	SRun2	SRun3	SRun4	SRun5
Yt_{peak}	8.0	8.0	8.0	10.0	12.0	10.0	8.0
Re_λ	72.6	101	112	107	88.0	132	110
$\langle u_1^2 \rangle / E_v$	0.53	0.50	0.53	0.59	0.65	0.58	0.54
$\langle u_2^2 \rangle / E_v$	0.16	0.20	0.18	0.16	0.11	0.17	0.18
$\langle u_3^2 \rangle / E_v$	0.31	0.30	0.29	0.25	0.24	0.25	0.28
$C(u_1, u_2)$	-0.57	-0.54	-0.56	-0.51	-0.36	-0.55	-0.55
E_m / E_v	0.031	0.128	0.747	0.089	0.030
$\langle b_1^2 \rangle / E_m$	0.48	0.65	0.84	0.58	0.47
$\langle b_2^2 \rangle / E_m$	0.23	0.15	0.06	0.23	0.23
$\langle b_3^2 \rangle / E_m$	0.29	0.20	0.10	0.19	0.30
$C(b_1, b_2)$	0.21	0.39	0.47	0.30	0.22

increased, while the correlation $C(b_1, b_2)$ displays the opposite behavior. The production terms in the mean kinetic and magnetic energy equations are related to these correlations and are proportional to $\langle u_1 u_2 \rangle$ and $\langle b_1 b_2 \rangle$, respectively. Hence, as the correlation $C(u_1, u_2)$ is decreased, the relative production of kinetic energy is also decreased and the turbulence grows at a slower rate. On the other hand, the relative increase of the magnetic Reynolds (Maxwell) stress component $\langle b_1 b_2 \rangle$ results in an increased relative production of magnetic energy. Note also that the correlations $C(u_1, u_2)$ and $C(b_1, b_2)$ have opposite signs. This is a result of the opposite sign of the source terms due to the mean velocity gradient in the transport equations of the fluctuating \mathbf{u} and \mathbf{b} fields.

Based on the previous discussions, it may be expected that the magnetic field, by damping the turbulence energy, should yield a lower Reynolds number. This, however, is not necessarily the case. Figure 7 illustrates this effect for both the ISO and the SHR cases. The ISO data show a transition at the critical box Reynolds number into distinct HD and MHD states. Above the critical value, a larger Re_λ is observed for the magnetic turbulence. The difference between these states increases as Re_0 increases. A similar trend is observed in the SHR flows. The Reynolds number is increased over its HD values (at the same Yt values) for all of the three simulations which are initialized with a 1% energy ratio (SRun1, SRun4, and SRun5). The obvious explanation for these trends is that the magnetic field, while decreasing the kinetic energy, also causes an increase in the length scales of the turbulence. However, if the initial magnetic field strength is large (SRun2 and SRun3), the kinetic energy can be damped sufficiently to result in a net decrease of the Reynolds number. The results for cases SRun5 and SRun1 again show similar trends; in the discussions below, case SRun5 is no longer considered.

The variation of the Taylor length scale is presented in Fig. 8 for both the ISO and the SHR flows. The Taylor scale is presented as the average over its value along all three directions. This average value is used in the SHR results as a representative length scale. In both flows, the length scale is observed to increase in the presence of a magnetic field. A similar behavior is observed for both the Kolmogorov and the integral length scales (not shown). In nonhelical MHD turbulence, a steepening of the kinetic energy spectrum in

the inertial range has been observed in EDQNM predictions.¹⁰ The integral length scales would be increased by this steepening. However, the enlargement of the Taylor scale is best explained in a structural sense as discussed below. The Taylor length scale in the MHD flows remain consistently larger than the HD case for the SHR flows except for the case with a 100% initial energy ratio (SRun3). In this case, the magnitude of the Lorentz force is of the same order as the pressure gradient. The initial magnetic field is uncorrelated with the velocity field, so that the Lorentz force acts as though it is a random forcing term applied as a step function at time $Yt=0$. This random force has the effect of initially increasing the relative amount of high wave-number energy, thus decreasing the length scales at early times.

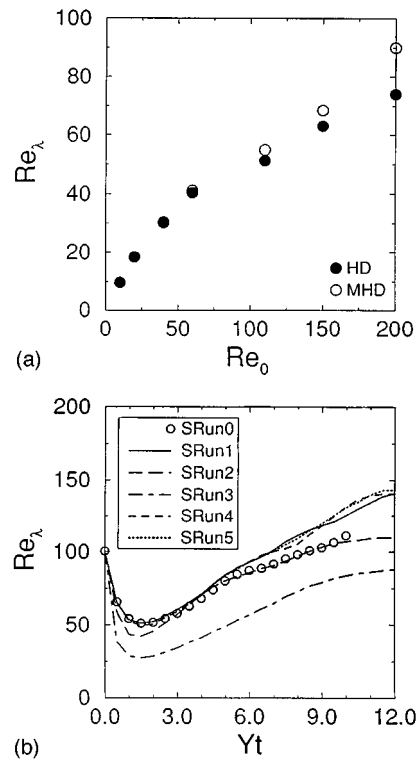


FIG. 7. Development of the Reynolds number based on the Taylor micro-scale (a) vs the box Reynolds number for the ISO simulations IRun0, 1, 5, 6, 7, 8, and 9 (right to left), (b) vs time for the SHR simulations.

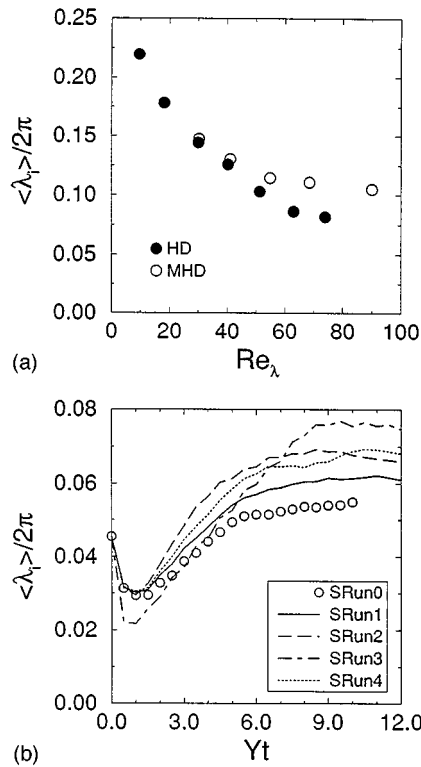


FIG. 8. Development of the Taylor length scale (a) for the ISO simulations IRun0, 1, 5, 6, 7, 8, and 9 (right to left) and (b) for the SHR simulations.

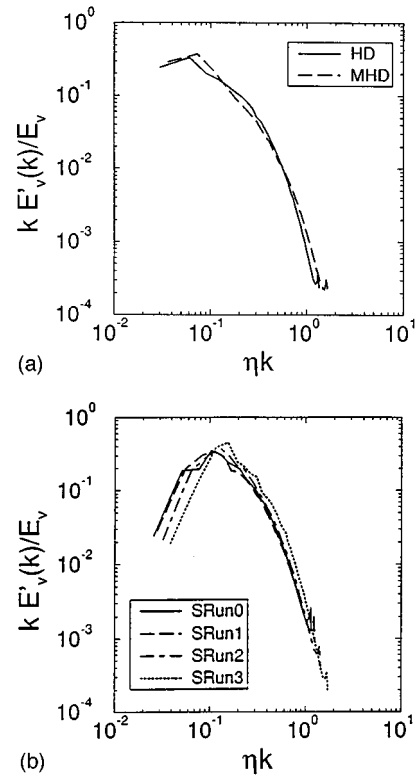


FIG. 9. Normalized energy spectra: (a) kinetic energy spectra for IRun0, (b) kinetic energy spectra for SHR flows. The ISO results are time averaged and the SHR results are for the peak times.

C. Energy spectra

Of primary concern in this section are the modifications of the HD spectra as caused by the magnetic field, and the relationship of the kinetic and magnetic spectra including equipartition. Equipartition refers to the tendency of MHD turbulence to develop nearly equal values for both the kinetic and magnetic energy at high wave numbers. This occurs due to the small scale exchange of energy between the two fields through the action of Alfvén waves. Figure 9 presents the normalized kinetic energy spectra for both the ISO and the SHR flows. The time averaged ISO spectra are taken from the high Reynolds number case IRun0. The SHR spectra are presented for cases SRUn0–SRUn3. These spectra are actually functions of the wave-number vector component for the anisotropic flow fields. However, in order to simplify the analysis, they are presented versus the wave-number magnitude. The SHR energy spectra are given for instantaneous flow conditions corresponding to the peak times. The primary effects of the magnetic field on the energy spectrum for the ISO data are to steepen the slope in the moderate wave-number region and to increase the relative energy in the high wave numbers [Fig. 9(a)]. There is no distinct inertial range at these Reynolds numbers. However, the steepening is in agreement with the EDQNM predictions.¹⁰ The Lorentz force creates a relative increase in the small scale energy of the turbulence. Of course, this is only a relative effect as the total energy is decreased. The SHR flows display this increase most significantly for case SRUn3 which displays the largest instantaneous energy ratio [Fig. 9(b)]. The dissipation spectra (not shown) for both flows display a mild flattening

in the moderate wave-number regions. The wave-number location of the maximum dissipation does not appear to change. The broadening effect implies that the transfer of the kinetic energy to the magnetic energy occurs over a relatively large range of scales and is centered around the scale corresponding to maximal viscous dissipation. The maximal magnetic and kinetic dissipation scales are approximately the same due to the unit magnetic Prandtl number considered here.

Examination of the equipartition effect is facilitated by the normalized kinetic and magnetic spectra in Fig. 10. Both energies are normalized by the kinetic energy to retain the relative crossing points. These results represent both relatively large and small E_m/E_v ratios for both flows. Parts (a) and (b) of Fig. 10 depict results of IRun0 and IRun6 with time averaged energy ratios of 0.16 and 0.023, respectively. The SHR spectra are shown in Figs. 10(c) and 10(d) for the instantaneous peak time data of simulations SRUn2 and SRUn1 with respective energy ratios of 0.128 and 0.031. The forms of both the kinetic and magnetic spectra remain approximately self-similar. However, the equipartition wave number is observed to migrate towards smaller wave numbers for larger energy ratios (i.e., from case IRun6 to IRun0 and from case SRUn1 to SRUn2). This migration also results in a magnetic field with a larger length scale. This was briefly discussed above in relation to the decreasing trends observed for the magnetic field intermittency with increasing energy ratios for $Re_\lambda > Re_{\lambda,c}$. Turbulence fields with larger length scales generally portray less intermittent effects. For

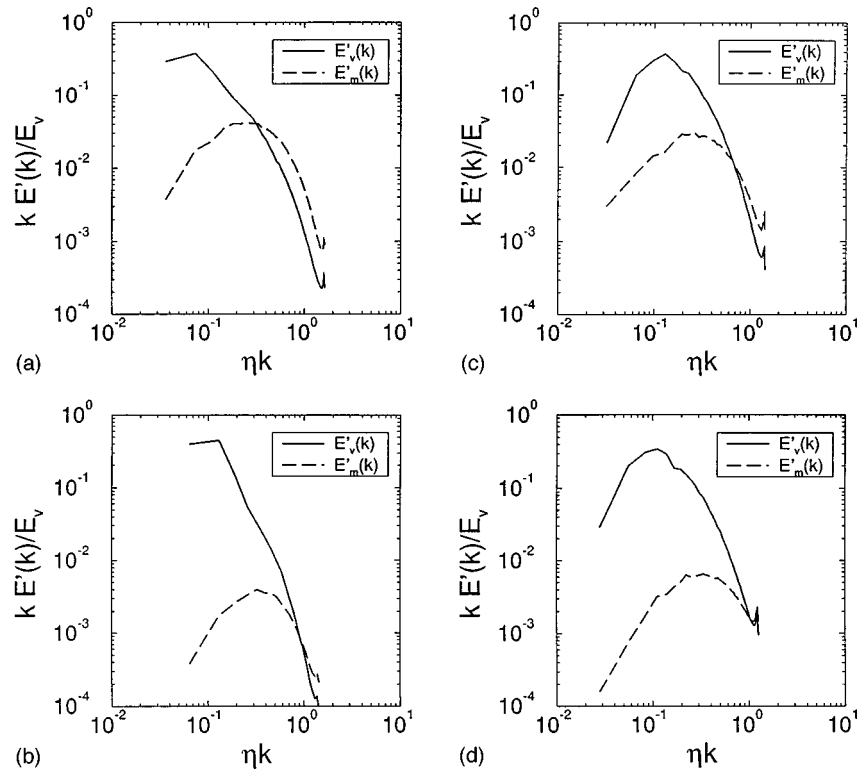


FIG. 10. Kinetic and magnetic energy spectra normalized by the mean turbulence energy: (a) IRun0, (b) IRun6, (c) SRUn2, and (d) SRUn1. The ISO results are time averaged and the SHR results are for the peak times.

example, passive scalar fields generally display asymptotic Gaussian statistics, but derivatives of the scalar are characterized by smaller length scales and portray significant departures from Gaussian.^{20,33} It is unknown whether the magnetic field intermittency will continue to decrease at larger Reynolds numbers (Fig. 5), and future simulations and/or experiments are needed to address this issue.

Another feature pertaining to energy spectra is found for ISO flows near the critical Reynolds number. The present results suggest that sustained dynamo action can occur in the absence of equipartition of high wave-number kinetic and magnetic energies. This is illustrated in Fig. 11 which depicts the normalized kinetic and magnetic energy spectra for the case IRun7. This is the lowest Reynolds number ISO simu-

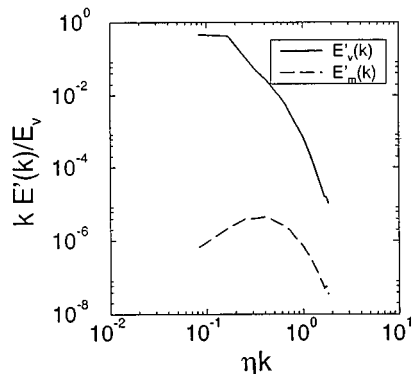


FIG. 11. Kinetic and magnetic energy spectra normalized by the mean turbulence energy for case IRun7.

lation for which a sustained dynamo action is observed. Notice that there is no equipartition of energy in this case; the magnetic energy spectrum appears to be “floating” nearly two decades beneath the kinetic spectrum. Any exchange of energy must be occurring through only very weak Alfvén waves. The simulation was conducted for more than 100 HD eddy turnover times and confirmed that the \mathbf{b} field is sustained. It may be possible for the equipartition to occur at very low energy values (at very high wave numbers). To capture the crossing point of the two spectra would require simulations with much higher resolution.

D. Structure and organization

This section is devoted to physical descriptions of coherency in 3-D nonhelical MHD turbulence. For this purpose, instantaneous fields from each of the cases IRun0 and SRUn2 are considered for detailed investigation. The results are considered at time $t/\tau_e = 25$ for the ISO data and at time $Yt = 10$ for the SHR data. Other simulated results from each configuration are confirmed to be in accord with the results presented for these two cases. Figure 12 illustrates the small scale structure of the ISO turbulence field. In Fig. 12(a) the vorticity field is highlighted with vorticity vectors in only the regions where the local vorticity magnitude is within 10% of its maximum value. As in the HD flow field, the high amplitude vorticity regions tend to organize into tube structures having thickness of the order of the Kolmogorov scale and length of the order of the integral scale. Figure 12(b) depicts magnetic field vectors in only the regions where the local magnetic field amplitude is within 10% of its maximum

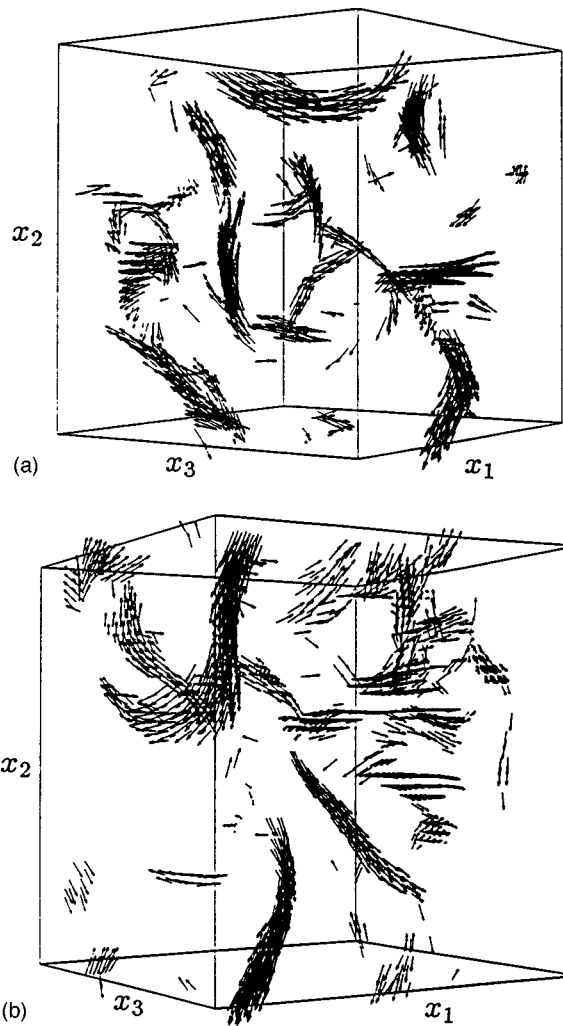


FIG. 12. Illustration of coherent structures in case IRun0 at time $t/\tau_e=25$ as depicted by vectors located in high amplitude regions: (a) vorticity vectors and (b) magnetic induction vectors.

value. The magnetic field also displays evidence of “tube-like” structures, hereinafter referred to as magnetic flux tubes. In contrast to the vorticity field, the magnetic field also shows a substantial tendency to align in “sheet-like” structures [the high amplitude induction regions at the upper right corner of Fig. 12(b) are confirmed with flow visualization as being sections of magnetic sheets]. Flow visualization shows that the regions of maximal current density are related more to the sheet structures than to the flux tubes. Both the vorticity and the induction fields are observed to be strongly intermittent. That is, the fields are concentrated in only a small fraction of the volume in physical space. No obvious correlation is observed between the two types of structures.

The vortical structure of homogeneous shear flows is known to be dominated by vortex tubes (aligned with the principal axis of the flow) which fold into the shape of a “horseshoe.” These structures are referred to as “hairpin” vortices.³⁰ Figure 13 shows the interaction of a typical hairpin vortex with a magnetic flux tube in the SHR flow. The structures are depicted with lines which are everywhere tangent to the vector of interest and which are concentrated only

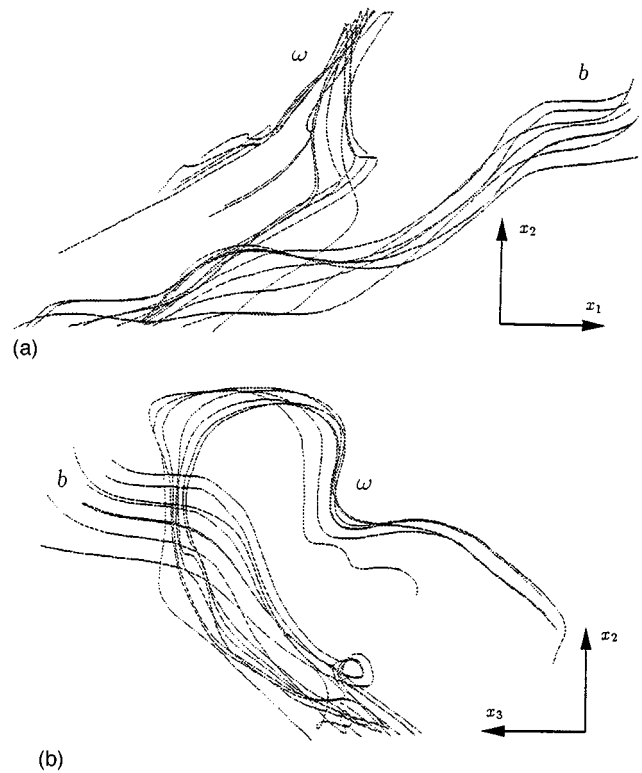


FIG. 13. Interaction of a vorticity hairpin vortex and a magnetic flux tube for case SRUn1 at time $Yt=8$: (a) spanwise view, and (b) streamwise view.

in regions of relatively high amplitude vorticity or magnetic field, respectively. Flow visualizations provide no evidence of magnetic hairpins. The magnetic flux tubes in the SHR flow show a tendency to align along directions close to the principal axis (45° in the x_1 - x_2 plane). Both the vorticity and the magnetic tube structures are of approximately the same length and width as those observed in the ISO flow.

The preferential alignment of the vorticity and the magnetic field vectors in the SHR flow is quantified with the inclination angle [$\theta = \tan^{-1}(v_2/v_1)$ for any vector v_i] of these vectors in the x_1 - x_2 plane. Figure 14 shows the distribution of this angle (the PDF of θ multiplied by 360°) for the vorticity field and also for several of the electromagnetic fields. The angle $\theta=0$ indicates the direction of positive x_1 (streamwise), with positive angles representing counter-clockwise rotation about the x_3 axis. The HD vorticity results are in agreement with the previous analysis of Rogers and Moin.³⁰ That is, there is peak alignment of the vorticity with the principal axis (45°) with equal relative weights for both positive and negative vorticity. The effect of the magnetic field is to skew the vorticity alignment towards the x_1 axis. This is explained by the alignment of the Lorentz force which acts perpendicularly to the \mathbf{b} field. The magnetic field and the Lorentz force show preferred angles approximately equal to 20° and -80° , respectively. The net effect is to force the vorticity vectors towards the x_1 axis.

The electromagnetic structure of several flux tubes was investigated via flow visualization. In general, these tubes were observed to have width on the order of the Kolmogorov scale and length on the order of the integral scale. The flux

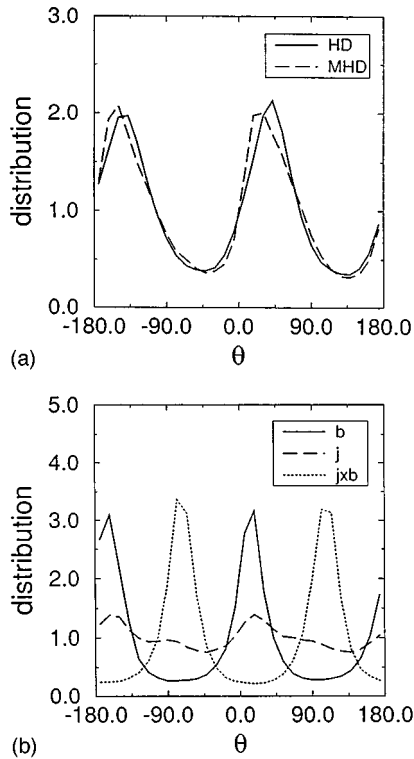


FIG. 14. Distribution of the inclination angle of the projection of vector fields in the x_1 - x_2 plane for case SRun1 at time $Yt=8$: (a) vorticity vector, (b) electromagnetic vectors.

tubes tend to repulse the local fluid by exerting a relatively strong Lorentz force on the fluid element radially away from themselves. This offers a possible explanation for the results of Fig. 4 which displays a large reduction in kinetic enstrophy for MHD turbulence, and may also explain the increase in turbulence length scales. Flux tubes forming in or near regions of large velocity gradients can act to “break up” these regions through the repulsive Lorentz action. This would have the effect of increasing the Kolmogorov scale and also decreasing the total kinetic enstrophy.

A more elaborate description of the small scale turbulence dynamics is achieved with the examination of the eigenvectors of the symmetric rate of strain tensor. Following the traditional notation, the eigenvalues are labeled as $\alpha \geq \beta \geq \gamma$, and the strain magnitude is denoted by S . In incompressible flows, $\alpha + \beta + \gamma = 0$, α is extensive, γ is compressive, and β has been shown to be typically extensive in HD turbulence (i.e., positive $\langle \beta \rangle$ values).^{34,35} The corresponding eigenvectors are denoted by \mathbf{e}_α , \mathbf{e}_β , and \mathbf{e}_γ , respectively. The typically extensive nature of the second eigenvalue is confirmed by the present MHD results. Table V lists the mean, the skewness, and the flatness for β/β_{rms} . The values correspond to instantaneous data of ISO simulation IRun0, and to the peak time data of SHR simulations SRun0 and SRun2. The middle eigenvalue of the magnetic field strain tensor $[s_{ij}^{(m)} = (b_{i,j} + b_{j,i})/2]$ is also included, and is denoted by β_m . The mean value for β remains positive; however, the magnitude is reduced for both of the MHD flows. This indicates a slight change in the small scale hydrodynamic structure of the MHD turbulence. In contrast to the

TABLE V. Statistics of the middle eigenvalue of the rate of strain tensors of both the velocity field (β) and the magnetic field (β_m), normalized by their respective standard deviations. IHD and SHD correspond, respectively, to HD results of IRun0 and SRun0 cases. IMHD and SMHD correspond, respectively, to MHD results of IRun0 and SRun2 cases.

	β (IHD)	β (SHD)	β (IMHD)	β (SMHD)	β_m (ISO)	β_m (SHR)
Mean	0.750	0.547	0.685	0.443	0.013	0.001
μ_3	1.17	0.838	1.31	1.41	0.030	0.046
μ_4	4.34	4.60	4.12	5.78	4.77	4.52

hydrodynamic field, β_m remains symmetrically distributed with near zero mean in both flows, and hence shows no tendency for either compressive or extensive character. This may be related to the lack of skewness for the longitudinal derivatives of the magnetic induction mentioned in Sec. III B, and also provides insight into the existence of both magnetic tube and sheet structures. Magnetic tube structures display two compressive magnetic strain eigenvectors ($\beta_m < 0$), whereas magnetic sheet structures are characterized by two extensive eigenvectors ($\beta_m > 0$).

Hereinafter, the analyses are limited to the IRun0 results, as the SHR results were observed to show similar trends. The PDF of the alignment of the vorticity vector with the electromagnetic fields is presented in Fig. 15. The magnetic field shows a strong tendency to align somewhat parallel to the vorticity vector. The vortex/flux tube interaction in Fig. 13 illustrates this effect, as the tails of the hairpin vortex are in the vicinity of the flux tube, where they run parallel to each other. The electric current running helically around the flux tubes would therefore be expected to show a preferred perpendicular alignment with the vorticity vector. However, Fig. 15 shows that no significant preferred alignment exists for these vectors. This can be explained in terms of the location of the strongest current magnitude within the flow field. As noted above, the strongest current regions are associated with the magnetic sheet structures which are correlated with the high strain regions of the flow, not the vorticity regions. This effect can be quantified by examining the statistics of the electromagnetic field conditioned on the second invariant of the deformation tensor:

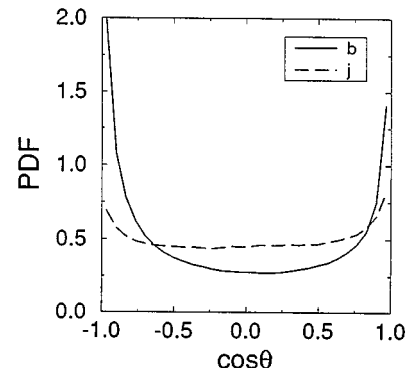


FIG. 15. PDF of the angle of alignment between the vorticity vector and the electromagnetic vectors. Case IRun0 at time $t/\tau_e=25$.

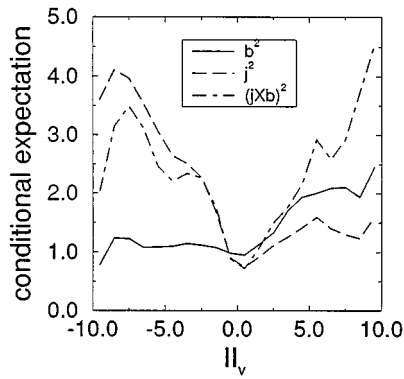


FIG. 16. Expected value of the squared magnitudes of the magnetic field, electric current, and the Lorentz force conditioned on the second invariant of the deformation tensor normalized by its standard deviation for simulation IRun0 at time $t/\tau_e=25$. The squared magnitudes are normalized by their expected values.

$$II_v = -\frac{1}{2} \frac{\partial u_i}{\partial x_j} \frac{\partial u_j}{\partial x_i} = -\frac{1}{2} \left(S^2 - \frac{1}{4} \omega_i \omega_i \right).$$

Therefore, the positive and negative values of II_v correspond to regions of high vorticity and high strain, respectively. Figure 16 presents the expectations of the squared magnitudes of the magnetic field, electric current, and the Lorentz force ($\mathbf{j} \times \mathbf{b}$), conditioned on the magnitude of the second invariant. The squared vector magnitudes are normalized by their mean values, and the second invariant is normalized by its standard deviation. Notice that there is a small tendency for the magnetic high amplitude regions to be located in regions of moderate to strong vorticity. However, these may only be relatively strong rotational fluid regions outside of the vortex tubes, as the flow visualization here (and that by Meneguzzi, Frisch, and Pouquet¹⁶) show no indication that these structures are correlated. Of more importance is the stronger correlation of the high amplitude current regions with the high strain regions of the flow. The current shows only moderate amplitudes in high vorticity regions, and hence no significant preferred alignment with the vorticity vector. The maximal regions of the Lorentz force are observed to be correlated with both high amplitude vorticity and high amplitude strain regions. Flow visualization also shows that regions of strong Lorentz force are associated with both the magnetic sheet structures (large strain) and the magnetic flux tubes (large vorticity).

The effects of the magnetic field on the hydrodynamics can be illustrated with the PDF of the alignment angle between the Lorentz force and various hydrodynamic vectors as presented in Fig. 17. In part (a) of the figure the entire field is considered, but in part (b) the angles are conditioned on only regions of the flow having a positive second invariant greater than three times its standard deviation. In this manner, the regions of predominantly vorticity tube structures are isolated. Note the change in the heights for the probabilities in the high vorticity regions. In agreement with the previously described parallel alignment of the \mathbf{b} and ω_i vectors, the Lorentz force is typically perpendicular to the vorticity and parallel to the kinetic pressure gradient. When conditioned on the high vorticity regions, the probability for

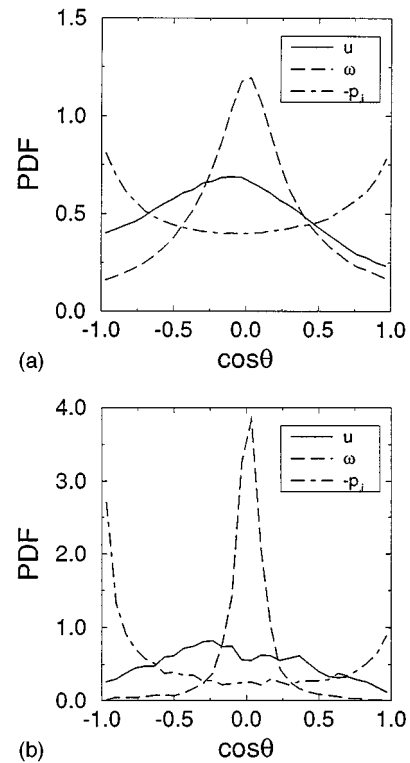


FIG. 17. PDF of the angle of alignment between the Lorentz force and the velocity, vorticity and negative of the kinetic pressure gradient: (a) the entire flow volume, (b) conditioned on regions where the second invariant is positive and larger than three times its standard deviation. Case IRun0 at time $t/\tau_e=25$.

these alignments becomes largely amplified. Also note that the PDF of the pressure gradient alignment in Fig. 17(b) is skewed towards antiparallel alignment. A phenomenological description of the vorticity tube structures can be made in which the low pressure vortical tubes are being broken up by the outward radial Lorentz force acting against the natural pressure gradient.

IV. SUMMARY AND CONCLUSIONS

Direct numerical simulations are conducted to study the small scale structure and dynamics of homogeneous nonhelical magnetohydrodynamic turbulence with unity magnetic Prandtl number. Both stationary isotropic and homogeneous shear flows are considered in both the presence and the absence of the magnetic field. The effects of the initial magnetic field conditions are examined and found to be somewhat insignificant for the stationary states of the isotropic flow. However, the homogeneous shear flow is significantly dependent on the initial conditions over the entire duration of the simulations. In particular, the initial length scale of the magnetic field is observed to influence the early time amplification of the field. This is due to a larger mean magnetic dissipation for initially small scale magnetic fields, and may result in an order of magnitude change in the ratio of magnetic to kinetic energy over the entire duration of the simulations.

Small scale dynamo action is observed in both flows. For the isotropic flow a critical Reynolds number of $Re_\lambda \approx 30$ is

found above which a stationary state is reached with a sustained magnetic field. For the range of parameters considered, the time averaged ratio of magnetic to kinetic energies scales nearly linearly with the Reynolds number. The homogeneous shear flow does not attain stationary states. However, monotonically increasing magnetic energies at late times indicate the presence of a dynamo effect. Although the magnetic energy is increasing, its ratio with the kinetic energy shows a decreasing trend. This is due to a larger time scale for the magnetic field response, as compared with the growth rate of the turbulence.

The simulation results reveal several modifications to the turbulence structure due to the presence of the magnetic field. In particular, in both flows the turbulence kinetic energy is decreased by the Lorentz force. However, except for very high amplitude initial magnetic fields in the shear flow simulations, the Taylor microscale Reynolds number is increased by the magnetic field. This occurs due to the enlargement of the hydrodynamic length scales. Also due to the magnetic field, the turbulence intermittency and the kinetic enstrophy are both observed to decrease, but the anisotropy is increased in shear flows. The induction is itself highly anisotropic in shear flows, and displays an off-diagonal magnetic Reynolds stress of opposite sign to the corresponding kinetic Reynolds stress.

Although the Reynolds numbers considered in the present simulations are not sufficiently large to produce discernible inertial ranges, many interesting features of the kinetic and magnetic energy spectra are portrayed. The kinetic energy spectra are shown to display increased relative high wave-number energy when a magnetic field is present. The crossing point of the normalized kinetic and magnetic energy spectra is observed to migrate towards the low wave numbers as the ratio of the magnetic energy to the kinetic energy is increased. Additionally, the wave number of the maximum kinetic energy increases with the increase of energy ratio.

The magnetic field is found to organize into both sheet- and tube-like structures. The regions of large magnetic field magnitude show a small correlation with the regions of moderate to large vorticity magnitude, and electric current structures are found to be correlated with the regions of large strain amplitude. The Lorentz force shows a strong tendency to align antiparallel with the pressure gradient force in the regions of strong vorticity. This has the effect of “breaking up” the turbulence structures and results in a decreased kinetic enstrophy. This structural description provides a physical interpretation of some of the above-mentioned phenomena.

ACKNOWLEDGMENTS

We are indebted to Dr. John Shebalin for many useful comments.

This work is part of an effort sponsored by the National Science Foundation under Grant No. CTS-9253488 and by the U.S. Office of Naval Research under Grant No. N00014-94-1-0667. Computational resources are provided by the School of Engineering and Applied Science Computing Center at SUNY—Buffalo and by the National Center for Supercomputing Applications at the University of Illinois at Urbana.

- ¹A. N. Kolmogorov, Dokl. Akad. Nauk SSSR, **30** (11), 301 (1941).
- ²D. Biskamp, *Nonlinear Magnetohydrodynamics* (Cambridge University Press, New York, 1993).
- ³G. K. Batchelor, Proc. R. Soc. London **201**, 405 (1950).
- ⁴J. H. Thomas, Phys. Fluids **11**, 1245 (1968).
- ⁵H. K. Moffatt, J. Fluid Mech. **53**, 385 (1972).
- ⁶A. Pouquet, U. Frisch, and J. Leorat, J. Fluid Mech. **77**, 321 (1976).
- ⁷D. Montgomery and T. Hatori, Plasma Phys. Controlled Fusion **26**, 717 (1984).
- ⁸W. H. Matthaeus, M. L. Goldstein, and S. R. Lantz, Phys. Fluids **29**, 1504 (1986).
- ⁹H. Chen and D. Montgomery, Plasma Phys. Controlled Fusion **29**, 205 (1987).
- ¹⁰J. Leorat, A. Pouquet, and U. Frisch, J. Fluid Mech. **104**, 419 (1981).
- ¹¹P. H. Roberts and T. H. Jensen, Phys. Fluids B **5**, 2657 (1993).
- ¹²P. Givi, Prog. Energy Combust. Sci. **15**, 1 (1989).
- ¹³P. Givi, in *Turbulent Reacting Flows*, edited by P. A. Libby and F. A. Williams (Academic, London, 1994), Chap. 8, pp. 475–572.
- ¹⁴A. Pouquet and G. S. Patterson, J. Fluid Mech. **85**, 305 (1978).
- ¹⁵P. A. Gillman and J. Miller, Astrophys. J. Suppl. **46**, 211 (1981).
- ¹⁶M. Meneguzzi, U. Frisch, and A. Pouquet, Phys. Rev. Lett. **47**, 1060 (1981).
- ¹⁷M. Meneguzzi and A. Pouquet, J. Fluid Mech. **205**, 297 (1989).
- ¹⁸D. Biskamp, H. Welter, and M. Walter, Phys. Fluids B **2**, 3024 (1990).
- ¹⁹U. Frisch, P. L. Sulem, and M. Nelkin, J. Fluid Mech. **87**, 719 (1978).
- ²⁰R. S. Miller, Ph.D. thesis, State University of New York at Buffalo, NY, 1995.
- ²¹A. Pouquet, P. L. Sulem, and M. Meneguzzi, Phys. Fluids **31**, 2635 (1988).
- ²²A. Orszag and C. M. Tang, J. Fluid Mech. **90**, 120 (1979).
- ²³S. Kida, S. Yanase, and J. Mizushima, Phys. Fluids A **3**, 457 (1991).
- ²⁴A. Nordlund, A. Brandenburg, R. L. Jennings, M. Rieutord, J. Ruokolainen, R. F. Stein, and I. Tuominen, Astrophys. J. **392**, 647 (1992).
- ²⁵A. Brandenburg, I. Procaccia, and D. Segel, Phys. Plasmas **2**, 1148 (1995).
- ²⁶J. V. Shebalin, W. H. Matthaeus, and D. Montgomery, J. Plasma Phys. **29**, 525 (1983).
- ²⁷S. Oughton, E. R. Priest, and W. H. Matthaeus, J. Fluid Mech. **280**, 95 (1994).
- ²⁸V. Eswaran, and S. B. Pope, Comput. Fluids **16**, 257 (1988).
- ²⁹R. S. Rogallo, *NASA Technical Memorandum 81315* (NASA Ames Research Center, Moffat Field, CA, 1981).
- ³⁰M. M. Rogers, and P. Moin, J. Fluid Mech. **176**, 33 (1987).
- ³¹Z. S. She, E. Jackson, and S. A. Orszag, Proc. R. Soc. London Ser. A **434**, 101 (1991).
- ³²D. Biskamp and U. Bremer, Phys. Rev. Lett. **72**, 3819 (1993).
- ³³F. Jaber, R. Miller, C. Madnia, and P. Givi, J. Fluid Mech. **313**, 241 (1996).
- ³⁴R. M. Kerr, Phys. Rev. Lett. **59**, 783 (1987).
- ³⁵W. T. Ashurst, A. R. Kerstein, R. M. Kerr, and C. H. Gibson, Phys. Fluids **30**, 2343 (1987).